

Quantum Learning and Estimation for Distribution Networks and Energy Communities Coordination

Yingrui Zhuang, Lin Cheng, *Senior Member, IEEE*, Yuji Cao,

Tongxin Li, *Member, IEEE*, Ning Qi, *Member, IEEE*, Yan Xu, *Senior Member, IEEE*, Yue Chen, *Member, IEEE*

Abstract—Price signals from distribution networks (DNs) guide energy communities (ECs) to adjust energy usage, enabling effective coordination for reliable power system operation. However, this coordination faces significant challenges due to the limited availability of information (i.e., only the aggregated energy usage of ECs is available to DNs), and the high computational burden of accounting for uncertainties and the associated risks through numerous scenarios. To address these challenges, we propose a quantum learning and estimation approach to enhance coordination between DNs and ECs. Specifically, leveraging advanced quantum properties such as quantum superposition and entanglement, we develop a hybrid quantum temporal convolutional network-long short-term memory (Q-TCN-LSTM) model to establish an end-to-end mapping between ECs' responses and the price incentives from DNs. Moreover, we develop a quantum estimation method based on quantum amplitude estimation (QAE) and two phase-rotation circuits to significantly accelerate the optimization process under numerous uncertainty scenarios. Numerical experiments demonstrate that, compared to classical neural networks, the proposed Q-TCN-LSTM model improves the mapping accuracy by 69.2% while reducing the model size by 99.75% and the computation time by 93.9%. Compared to classical Monte Carlo simulation, QAE achieves comparable accuracy with a dramatic reduction in computational time (up to 99.99%) and requires significantly fewer computational resources.

Index Terms—Quantum neural network, quantum amplitude estimation, energy communities, distribution networks, coordination

I. INTRODUCTION

WITH the rapid development of distributed energy resources (DERs), traditional centralized power systems are gradually evolving toward a more distributed architecture. Energy communities (ECs), which integrate various types of DERs, are playing a vital role in enhancing the local supply-demand balance and improving energy utilization efficiency [1].

This work is supported in part by 1+1+1 CUHK-CUHK(SZ)-GDST Joint Collaboration Fund (No. GRDP2025-055), National Natural Science Foundation of China (No. 52037006), the CUHK Strategic Partnership Award for Research Collaboration (No. 4750467), and China Postdoctoral Science Foundation special funded project (No. 2023TQ0169). (*Corresponding author: Yue Chen.*)

Yingrui Zhuang and Lin Cheng are with the Department of Electrical Engineering, Tsinghua University, Beijing 100084, China (e-mail: zyr21@mails.tsinghua.edu.cn).

Yue Chen and Yuji Cao are with the Department of Mechanical and Automation Engineering, The Chinese University of Hong Kong, Hong Kong SAR, China (e-mail: yuechen@mae.cuhk.edu.hk, yjcao@mae.cuhk.edu.hk).

Tongxin Li is with the School of Data Science, The Chinese University of Hong Kong (Shenzhen), Shenzhen China. (email: litongxin@cuhk.edu.cn).

Ning Qi is with the Department of Earth and Environmental Engineering, Columbia University, NY 10027, USA (e-mail: nq2176@columbia.edu).

Yan Xu is with the School of Electrical and Electronic Engineering, Nanyang Technological University, Singapore 639798, Singapore. (email: xuyan@ntu.edu.sg).

In this context, achieving coordinated operation between distribution networks (DNs) and ECs is essential for enhancing system flexibility and reducing risks [2]. To this end, leveraging price incentives provided by DNs to generate grid-supportive responses of ECs is one of the effective approaches to facilitate such coordination.

However, two critical challenges remain in achieving effective DNs-ECs coordination. The first challenge is that accurate estimation of ECs' electricity consumption behavior remains difficult [3]. In some literature, an ideal assumption is made that the DNs have full access to ECs' internal data (e.g., device parameters, operational states, and operational preferences). Thus, detailed operational models of ECs can be constructed based on physical modeling of devices, such as modeling electro-thermal coupling of air conditioners [4] and industrial production processes [5]. Moreover, to improve the overall computational tractability, simplified convex models were built and embedded into the centralized optimization model within the DNs [6]. However, in real-world situations, user electricity consumption behaviors usually exhibit strong nonlinearity, non-stationarity, and partial irrationality [7], making convex models inaccurate. Moreover, ECs are often unwilling or unable to share the device-level data due to privacy concerns, cybersecurity risks, or commercial interests [8], making the development of detailed user-side models impractical. Under such restrictions, DNs often can only access the aggregated energy usage of ECs, without insight into detailed device configurations or usage patterns [9]. To address this issue, distributed optimization methods (e.g., alternating direction method of multipliers [10]) have been widely adopted, where the centralized optimization problem is decomposed into several subproblems that are solved independently. While such methods offer good privacy protection, they often suffer from heavy communication burdens and slow convergence. Alternatively, some studies have proposed data-driven approaches to construct surrogate models that emulate user electricity consumption behaviors in response to external incentives [11]. However, such behavioral modeling is essentially a time-series analysis problem characterized by high dimensionality, temporal variability, and strong nonlinearity, leading to high learning complexity. In particular, for ECs with complex operational characteristics, achieving high behavioral modeling accuracy often requires a large number of model parameters [12], which further increases model complexity and reduces computational efficiency.

The second challenge arises from the reliance on a large number of scenarios to characterize uncertainty-related risks [13] when precise probabilistic distributions are

unavailable. For instance, conditional value-at-risk (CVaR)-based risk models require an accurate representation of the tail of distributions [14], which necessitates a large set of scenarios to capture the rare but high-impact events. Monte Carlo (MC) simulation is commonly employed to evaluate the expectation across a broad range of possible scenarios [15]. Nevertheless, MC methods often suffer from low computational efficiency and slow convergence. To reduce computational complexity, scenario reduction techniques have been explored to compress the original large-scale scenario set into a smaller yet representative subset [16]. However, for tail-sensitive risk measures such as CVaR, scenario reduction methods may not be able to fully preserve the integrity of the tail of distributions, leading to loss of valuable information and degraded risk awareness.

Recent advances in quantum computing have opened up new opportunities for effective DNs-ECs coordination. Unlike classical computing, which processes information sequentially and requires large parameter sets to model complex systems, quantum computing leverages quantum superposition and entanglement properties inherent in quantum bits (qubits), allowing the representation and manipulation of an exponential number of states simultaneously with fewer parameters [17]. On the hardware front, companies such as IBM and Google have developed prototype systems with tens to hundreds of qubits, signaling the advent of the Noisy Intermediate-Scale Quantum (NISQ) era [18]. These developments make quantum computing particularly suitable for solving problems characterized by high dimensionality, complex data structures, and intensive computational demands with inherent parallelism.

For the first challenge of estimating electricity consumption behavior of ECs, quantum neural networks (QNNs) offer a promising solution to establish the mapping between external incentives and ECs' responses. Compared to classical neural networks, QNNs use qubits and quantum gates to perform computations in a superposed and entangled state, offering potential advantages in representing complex nonlinear relationships and accelerating the training process. Existing studies have applied QNNs to various power system-related tasks, such as wind speed forecasting [19], carbon price forecasting [20] and fault diagnosis [21]. However, the ECs incentive-response mapping problem incorporates ECs' operational characteristics and constitutes a more complex temporal regression task. Simplified QNNs in current studies lack the capacity to sufficiently capture the intricate temporal and coupled dependencies inherent to ECs' operation.

For the second challenge of computational bottlenecks arising from large-scale scenario analysis, quantum estimation methods (e.g., quantum amplitude estimation, QAE) provide a promising solution. Compared to classical MC methods, QAE theoretically achieves a quadratic speedup [22], [23], demonstrating significant advantages in key subroutines such as expectation evaluation and CVaR computation [24]. Refs [25], [26] have applied QAE to power system reliability assessment, validating its potential in uncertainty-aware analysis. Most current research has focused on the theoretical feasibility of QAE algorithms, with limited discussions on the practical quantum circuit design. Therefore, a key challenge lies in designing task-specific quantum circuits that balance

estimation accuracy and computational complexity to enable rapid and precise evaluation of uncertainty scenarios.

In this paper, we propose a quantum learning and estimation method for the coordinated operation of DNs and ECs. Our main contributions are as follows:

- 1) We develop a hybrid quantum temporal convolutional network–long short-term memory (Q-TCN-LSTM) model to estimate the energy consumption behavior of ECs in response to the price incentives from the DNs. To the best of our knowledge, the Q-TCN-LSTM model has not been explored in prior research. Q-TCN and Q-LSTM respectively extract short-term and long-term temporal dependencies, comprehensively modeling the coupled temporal dependencies of incentive-response characteristics of ECs. Compared to the classical TCN-LSTM, Q-TCN-LSTM improves accuracy by 69.2%, while reducing model size by 99.75% and computation time by 93.9%.
- 2) We develop a quantum amplitude estimation method to address the computational burden of estimating the gradient of CVaR under a large number of uncertainty scenarios, which is a critical component in DNs–ECs coordination. Two phase rotation circuits are introduced: one establishes analytical linear approximations between rotation angles and quantum states, achieving low circuit complexity but with potential approximation errors; the other computes exact rotation angles which are adaptively applied by introducing additional qubits, ensuring high accuracy but with increased complexity. Compared to the classical MC simulation, the proposed quantum estimation method achieves comparable accuracy with a dramatic reduction in computational time (up to 99.99%).

The rest of the paper is organized as follows. Section II introduces the coordination problem formulation between DNs and ECs. The methodology of the proposed quantum learning and estimation approach is presented in Section III. Numerical case studies are provided in Section IV. Finally, we summarize our conclusion in Section V.

II. PROBLEM FORMULATION

A. DNs-ECs Coordination Structure

The structure of DNs integrated with multi-type ECs and DERs (e.g., wind turbines (WT), photovoltaic (PV) systems, and new-type loads) is illustrated in Fig. 1. This paper focuses on three representative types of ECs: residential, commercial, and industrial.

In this paper, we focus on the day-ahead price-incentive demand response mechanism as a coordination strategy, wherein price signals guide ECs to adjust their operations accordingly. The coordination between DNs and various ECs is naturally a bilevel optimization problem, with DNs making decisions at the upper level and ECs responding at the lower level. At the upper level, DNs should accurately estimate the uncertainty associated with renewable energy sources (RESs), loads, and the trading power of ECs, and accordingly make risk-averse operational decisions, which is mainly considered as the price signals for ECs. At the lower level, each EC independently optimizes its operational strategy based on customized

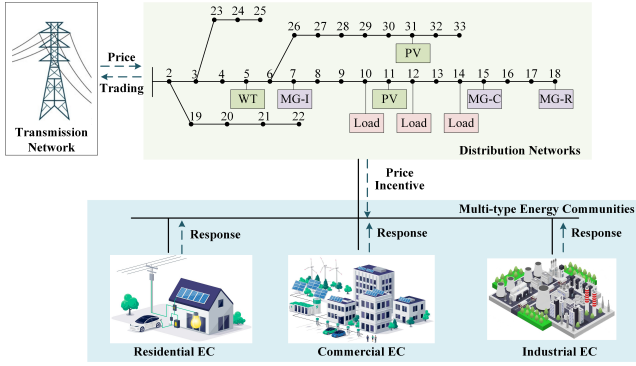


Fig. 1. Coordination structure between DN and multi-type ECs.

operational objectives in response to the price signals from the DNs, and submits the resulting power trading plans to the DNs.

B. Risk-Averse Operation Model of Distribution Networks

Considering the uncertainty in load and RESs, DNs need to make risk-averse decisions to reduce the operational risks including voltage violations and line overloads. In this paper, CVaR is adopted to quantify operational risk, where the uncertainties in load and RESs are modeled using a set of discrete scenarios. Accordingly, the overall operation model of the DNs is formulated as follows:

$$\min C = \sum_{s=1}^S \gamma_s f(z, \xi_s) + \lambda(v_\alpha + \frac{1}{1-\alpha} \sum_{s=1}^S \gamma_s [f(z, \xi_s) - v_\alpha]_+), \quad (1a)$$

$$\text{s.t. } f(z, \xi_s) = \sum_{t=1}^T \Delta t [- \sum_{i \in \Omega^B} \pi_t^{\text{EC}} P_{i,t}^{\text{EX,EC}} + \pi_t^{\text{DN}} P_{s,t}^{\text{EX,DN}} + \beta_1 \sum_{i \in \Omega^B} ([V_{i,s} - \bar{V}]_+ + [\bar{V} - V_{i,s}]_+) + \beta_2 \sum_{ij \in \Omega^L} (P_{ij,s,t} - \bar{P}_{ij})], \quad (1b)$$

$$\mathcal{V}_{j,s,t} = \mathcal{V}_{i,s,t} - 2(r_{ij} P_{ij,s,t} + x_{ij} Q_{ij,s,t}), \quad (1c)$$

$$p_{j,s,t} = P_{ij,s,t} - \sum_{l:j \rightarrow l} P_{jl,s,t}, \quad (1d)$$

$$q_{j,s,t} = Q_{ij,s,t} - \sum_{l:j \rightarrow l} Q_{jl,s,t}, \quad (1e)$$

$$p_{j,s,t} = -P_{j,s,t}^{\text{R}} + P_{j,s,t}^{\text{L}} + P_{j,t}^{\text{EX,EC}}, \quad (1f)$$

$$q_{j,s,t} = Q_{j,s,t}^{\text{L}} + Q_{j,t}^{\text{EX,EC}}, \quad (1g)$$

$$P_i^{\text{EX,EC}} = \phi_i(\pi^{\text{EC}}), \quad (1h)$$

$$\underline{\pi}_t^{\text{EC}} \leq \pi_t^{\text{EC}} \leq \bar{\pi}_t^{\text{EC}}, \quad (1i)$$

$$\frac{1}{T} \sum_{t=1}^T \pi_t^{\text{EC}} = \pi_t^{\text{EC,av}}, \quad (1j)$$

where (1c)-(1e) are the linearized distflow model. (1f)-(1g) are the power injection constraints. (1i)-(1j) are the price signal constraints. ξ_s is the s -th scenario (S in total) with probability γ_s . $f(z, \xi_s)$ is the cost under the s -th scenario, where z denotes the decision variables of DNs. $P_{i,t}^{\text{EX,EC}}$ is the active trading power between the EC at node i and DNs, which is the EC's

response to the price signal π_t^{EC} . Note that the DNs do not know the exact operation patterns and device parameters of ECs, we adopt a unknown function $\phi_i(\cdot)$ to represent the corresponding response characteristics, as in (1h). The active and reactive trading power of ECs are assumed to be proportional, with the fixed ratio given by $P_{i,t}^{\text{EX,EC}}/Q_{i,t}^{\text{EX,EC}} = \kappa_i$. λ is the risk aversion coefficient which controls the risk acceptance level. v_α is the VaR at the α -th percentile. $[z]_+ = \max(0, z)$. π_t^{DN} is the trading price published by the transmission network to DNs. $P_{s,t}^{\text{EX,DN}}$ is the trading power of the DNs with the transmission network under scenario s at time t . π_t^{EC} is limited by $\bar{\pi}_t^{\text{EC}}/\underline{\pi}_t^{\text{EC}}$, and averaged by $\pi_t^{\text{EC,av}}$. β_1/β_2 are the penalty coefficients of the voltage and line power flow violations. $V_{i,s}$ is the voltage magnitude limited by \bar{V}/\underline{V} . $P_{ij,s,t}/Q_{ij,s,t}$ are the active/reactive power flow of line ij . r_{ij}/x_{ij} are the resistance/reactance. $p_{j,s,t}/q_{j,s,t}$ are the active/reactive power injection. $P_{j,s,t}^{\text{R}}$ is the active power output of RESs at bus j under scenario s at time t . $P_{j,s,t}^{\text{L}}/Q_{j,s,t}^{\text{L}}$ are the active/reactive power loads. In (1f), $P_{j,s,t}^{\text{R}} = 0$ and $P_{j,s,t}^{\text{EX,EC}} = 0$ if bus j is not connected to any RES or EC, respectively.

C. Incentive-Response Mapping Integrated Gradient Descent for DNs-ECs Coordination

Under limited availability of information, DNs can only access the aggregated energy usage of each EC, while the detailed internal data and operational states of ECs remain unobservable. Therefore, the bilevel DNs-ECs coordination problem cannot be solved directly. To address this challenge, we propose to learn a direct mapping that captures the incentive-response behavior of ECs, as in (2).

$$\hat{P}_i^{\text{EX,EC}} = \varphi_i(\pi^{\text{EC}}; \Theta) \sim \phi_i(\pi^{\text{EC}}), \quad (2)$$

where the parameters Θ can be optimized by minimizing a loss function (e.g., mean square error, MSE):

$$\Theta^* = \operatorname{argmin}_{\Theta} \frac{1}{T} \sum_{t=1}^T (P_t^{\text{EX,EC}} - \hat{P}_t^{\text{EX,EC}})^2. \quad (3)$$

Then, by using the mapping model in (2) to replace the unknown response function in (1h), the original bilevel DNs-ECs coordination problem is reformulated as a single-level optimization problem, yielding solutions equivalent to those of the original bilevel formulation.

With the differentiability of the mapping model (2), the integrated DNs Optimization model is differentiable and solvable via gradient-based methods. With respect to the decision variables z and v_α of DNs optimization, the gradient descent update rule can be expressed as:

$$z^{k+1} = z^k - \eta \frac{\partial C}{\partial z^k}, \quad v_\alpha^{k+1} = v_\alpha^k - \eta \frac{\partial C}{\partial v_\alpha^k}, \quad (4a)$$

$$\frac{\partial C}{\partial z} = \sum_{s=1}^S \gamma_s \frac{\partial f(z, \xi_s)}{\partial z} + \lambda \frac{1}{1-\alpha} \sum_{s=1}^S \gamma_s \frac{\partial f(z, \xi_s)}{\partial z} I(f(z, \xi_s) > v_\alpha), \quad (4b)$$

$$\frac{\partial C}{\partial v_\alpha} = \lambda \left(1 - \frac{1}{1-\alpha} \sum_{i=1}^N \gamma_s I(f(z, \xi_s) > v_\alpha) \right), \quad (4c)$$

where $I(f(z, \xi_s) > v_\alpha) = 1$ if $f(z, \xi_s) > v_\alpha$ else 0.

Notably, two main challenges exist in (4):

- 1) The response behavior of ECs should be accurately estimated in (2). However, this task constitutes a complex long-horizon temporal sequence modeling problem, which poses significant challenges regarding both accuracy and generalizability.
- 2) To compute (4), numerous scenarios are required to achieve accurate risk quantification, which leads to a heavy computational burden.

In the next section, inspired by the recent advances in quantum computing, we propose a quantum learning and estimation approach to address the above two challenges, thus facilitating efficient DNs-ECs coordination.

III. METHODOLOGY OF QUANTUM LEARNING AND ESTIMATION

In this section, we introduce the proposed quantum learning and estimation approach. Specifically, a Q-TCN-LSTM model is proposed to learn the incentive-response characteristics of ECs. Subsequently, a quantum estimation method is developed to accelerate the gradient computation across numerous scenarios.

A. Structure of Q-TCN-LSTM

Generally, QNNs are built on trainable variational quantum circuits (VQCs), which consist of layered arrangements of parameterized quantum gates, leveraging quantum properties such as superposition and entanglement. In this part, we first present the fundamental structure of VQCs. Then, we introduce the proposed Q-TCN-LSTM model.

1) *Variational Quantum Circuits*: A VQC is generally composed of three main components: quantum state preparation, parameterized variational circuits and quantum measurement, as illustrated in Fig. 2.

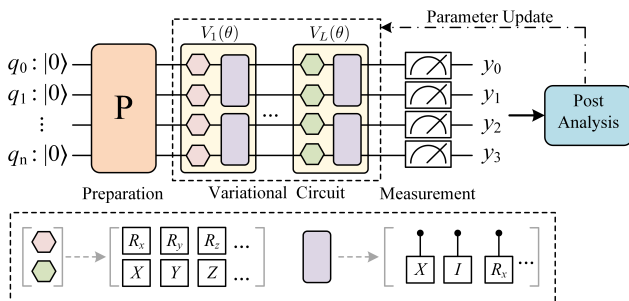


Fig. 2. General structure of variational quantum circuits.

Firstly, the quantum state preparation block \mathbf{P} embeds the classical data into quantum states:

$$|\psi_0\rangle_n = \sum_{i=0}^{2^n-1} \alpha_i |i\rangle_n, \quad (5)$$

where $|\psi_0\rangle_n$ represents the initial quantum state of n qubits; $|i\rangle_n$ is the i -th basis state in the 2^n -dimensional Hilbert space, associated with amplitude α_i and a measurement probability of α_i^2 , which satisfies $\sum_{i=0}^{2^n-1} \alpha_i^2 = 1$. At this stage, VQC encodes exponentially many states via quantum superposition,

thereby offering computational advantages in high-dimensional problems.

Secondly, the parameterized variational circuit block $V(\theta)$ applies a sequence of complex unitary transformations on $|\psi_0\rangle_n$. Single-bit gates (e.g., Pauli-X gate, rotation gate) and multi-bit gates (e.g., controlled-NOT gate, controlled-rotation gate) are used to manipulate the quantum state, collectively inducing quantum entanglement and further exploiting the superposition across qubits. This process enables the circuit to represent intricate nonlinear dependencies inherent in the input data. Usually, the variational circuit is composed of L layers, each consisting of a set of parameterized or fixed single-qubit gates and entangling gates, forming the overall unitary:

$$V(\theta) = \prod_{l=1}^L (V_{(l)}^{\text{ent}} \cdot V_{(l)}^{\text{rot}}(\theta_{(l)})), \quad (6)$$

where $V_{(l)}^{\text{ent}}$ is the entangling gate at layer l , $V_{(l)}^{\text{rot}}(\theta_{(l)}) = \bigotimes_{i=1}^n R_{(x,y,z)}(\theta_{(l),i})$ is the rotation gate at layer l . With the variational circuit, the quantum state is transformed as:

$$|\psi(\theta)\rangle_n = V(\theta)|\psi_0\rangle_n. \quad (7)$$

Finally, the measurement block performs projective measurements on $|\psi(\theta)\rangle_n$:

$$\langle \mathcal{O} \rangle_\theta = \langle \psi(\theta) | \mathcal{O} | \psi(\theta) \rangle_n. \quad (8)$$

where $\langle \psi(\theta) |$ is the conjugate transpose of $|\psi(\theta)\rangle$. Equation (8) denotes the expectation value of the observable Hermitian operator \mathcal{O} , resulting in classical scalar values for post analysis.

The measurement output $\langle \mathcal{O} \rangle_\theta$ represents a highly nonlinear transformation of the input, implicitly capturing complex correlations encoded by the VQC. The parameters θ are optimized via classical optimization algorithms (e.g., Adam) to minimize a predefined loss function. Leveraging quantum parallelism and entanglement, VQCs can model complex patterns with significantly fewer trainable parameters compared to classical neural networks.

2) *Structure of Q-TCN-LSTM*: In response to time-varying electricity price signals, ECs exhibit both short-term (spanning several hours) response characteristics, and long-term (over the scheduling horizon) globally optimal decision-making. Therefore, a coupling relationship exists between the response of ECs and price incentives in both the short and long term. To capture this coupling, we propose a quantum-enhanced hybrid architecture, Q-TCN-LSTM, which integrates the advantages of temporal convolutional networks (TCNs) and long short-term memory (LSTM) networks. Specifically, TCNs can efficiently extract short-term features from time series data through causal and dilated convolution mechanisms. Meanwhile, LSTM can store long-term information in their cell states and selectively remember or forget information through gating mechanisms, effectively capturing long-term dependencies in time series. Fully connected (FC) layers then map the extracted features to the final output. The overall structure of the proposed Q-TCN-LSTM model is shown in Fig. 3.

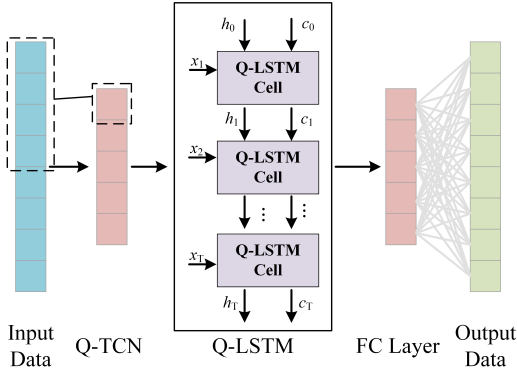


Fig. 3. Structure of Q-TCN-LSTM.

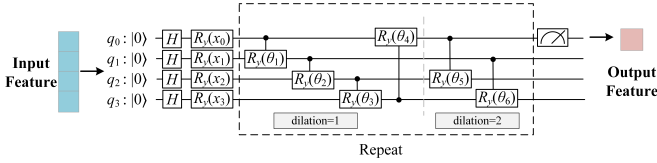


Fig. 4. Structure of 4-qubit VQC for Q-TCN.

3) Q-TCN for Short-Term Temporal Feature Extraction:

Based on the classical TCN, we integrate VQCs into the causal convolutions to construct a quantum TCN (Q-TCN) model. For instance, a 4-qubit VQC for Q-TCN is illustrated in Fig. 4.

The proposed Q-TCN model efficiently captures temporal correlations and complex nonlinear relationships across multiple time steps by embedding classical time-series data into a quantum feature space, leveraging quantum superposition and entanglement. Specifically, Q-TCN utilizes a temporal rotational encoding scheme, where each input value x_t is mapped to the angle of a rotation gate. This encoding preserves local temporal patterns while mitigating potential information loss commonly associated with sparse sampling in classical TCNs. Then, a parameterized variational circuit with skip-connected entanglement gates performs entanglement across temporally aligned qubits, constructing temporal dependencies without deep stacking or activations in classical TCNs. Finally, quantum measurements produce output features that capture interactions across multiple time steps. Quantum properties such as superposition and entanglement enhance Q-TCN's expressive power with significantly fewer trainable parameters, effectively reducing model redundancy.

4) *Quantum LSTM for Long-Term Temporal Feature Extraction:* Based on the classical LSTM architecture, we construct a quantum LSTM (Q-LSTM) model by replacing the gate mechanisms with VQCs, as illustrated in Fig. 5.

The corresponding forward pass equations in a compact form are as follows:

$$v_t = [h_{t-1}, x_t], \quad (9a)$$

$$f_t = \sigma(VQC_1(v_t)), \quad (9b)$$

$$i_t = \sigma(VQC_2(v_t)), \quad o_t = \sigma(VQC_4(v_t)), \quad (9c)$$

$$c_t = f_t \otimes c_{t-1} + i_t \otimes \tilde{c}_t, \quad \tilde{c}_t = \tanh(VQC_3(v_t)), \quad (9d)$$

$$h_t = VQC_5(o_t \otimes \tanh(c_t)), \quad y_t = VQC_6(h_t), \quad (9e)$$

where σ and \tanh blocks represent the sigmoid and

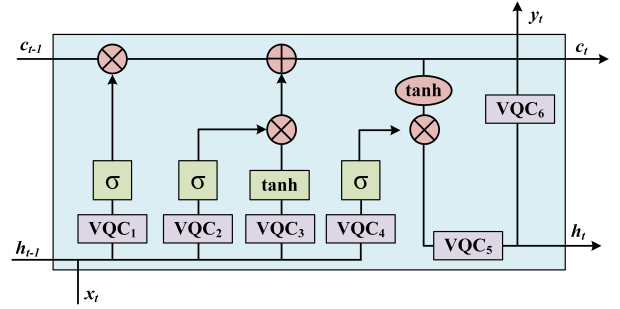


Fig. 5. Structure of Q-LSTM cell.

the hyperbolic tangent activation function, respectively. $x_t/h_t/c_t/y_t$ are the input, hidden state, cell state, and output at time t . \otimes and \oplus represents element-wise multiplication and addition. $[\cdot]$ represents the vector concatenation, f_t, i_t, o_t represent the forget gate, input gate, and output gate in the LSTM model, respectively.

B. Quantum Amplitude Estimation

In (1a) and (4), a large number of scenarios are required for precise risk quantification, which introduces considerable computational complexity. Classical approaches typically rely on MC simulation for estimation, which has been verified to require $\mathcal{O}(1/\varepsilon^2)$ samples to achieve an estimation error of ε . This leads to substantial computational overhead. Alternatively, quantum amplitude estimation, leveraging quantum entanglement and amplitude amplification, can theoretically achieve the same precision level ε with only $\mathcal{O}(1/\varepsilon)$ queries [27], offering a theoretical quadratic speedup compared to MC. Next, we propose a quantum estimation method for efficient computation of (4). Take the first term in (4) (i.e., $\sum_{s=1}^S \gamma_s \frac{\partial f(x, \xi_s)}{\partial x}$) as an example. We rewrite it as $\sum_{s=1}^S p(\xi_s) \hat{f}(\xi_s)$ and suppose ξ follows distribution \mathcal{X} . The QAE procedure generally involves three steps:

Step 1-Quantum State Preparation: \mathcal{X} is divided into $N=2^n$ intervals, and is embedded into a quantum state:

$$|\psi\rangle_n = \sum_{i=0}^{N-1} \sqrt{p_i} |i\rangle_n, \quad (10)$$

where $|i\rangle_n$ represents a basis state of n qubits, p_i is the probability of state $|i\rangle_n$ with $\sum_{i=0}^{N-1} p_i = 1$. Common strategies for quantum state preparation include angle encoding, amplitude encoding, and basis encoding. In the uniform case where $p_i = 1/N \forall i \in [0, \dots, N-1]$, (10) can be efficiently prepared using Hadamard gates.

Step 2-Quantum State Rotation: Assuming a function $\hat{f}: \{0, 1, \dots, 2^n - 1\} \rightarrow [0, 1]$, a controlled rotation operator \mathcal{F} is constructed such that

$$\mathcal{F}|i\rangle_n|0\rangle = \sqrt{1-\hat{f}(i)}|i\rangle_n|0\rangle + \sqrt{\hat{f}(i)}|i\rangle_n|1\rangle. \quad (11)$$

Applying \mathcal{F} to $|\psi\rangle_n$ yields

$$\mathcal{F}|\psi\rangle_n|0\rangle = \sum_{i=0}^{N-1} \sqrt{(1-\hat{f}(i))p_i} |i\rangle_n|0\rangle + \sum_{i=0}^{N-1} \sqrt{\hat{f}(i)p_i} |i\rangle_n|1\rangle. \quad (12)$$

In the implementation of \mathcal{F} , the auxiliary qubit undergoes a rotation $R_y(\theta)$ with $\theta = 2\arcsin(\sqrt{\hat{f}(i)})$. In our case, $\hat{f}(\xi)$ is a linear function of ξ , i.e., $\hat{f}(\xi) = a\xi + b$. Thus, $\theta = 2\arcsin(\sqrt{a\xi + b})$, which is nonlinear with respect to ξ . Depending on the trade-off between circuit complexity and estimation accuracy, we propose two potential implementations of \mathcal{F} .

The first circuit implementation, referred to as Circuit-1, employs analytical approximations of the nonlinear rotation and emphasizes low circuit complexity, as illustrated in Fig. 6. Assuming x is sufficiently small, we have $\arcsin(\sqrt{x}) \approx cx + d$, where c and d can be obtained via the least squares method. To conform to this approximation regime, a linear transformation can be applied to the function $\hat{f}(\xi)$, such that $\theta \approx \hat{a}\xi + \hat{b}$. Under this condition, the controlled rotation operator \mathcal{F} can be efficiently realized using a series of parameterized controlled-RY gates, with low implementation complexity.

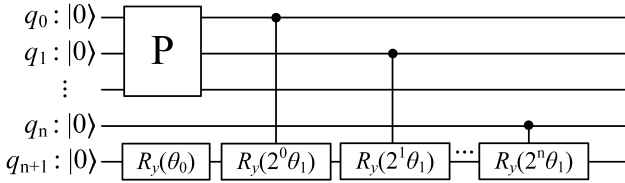


Fig. 6. Circuit-1 for approximated implementation of \mathcal{F} .

The second circuit implementation, referred to as Circuit-2, computes the exact nonlinear rotation angle corresponding to each quantum basis state. To this end, we design a rotation-angle-adaptive circuit architecture. In this scheme, n original qubits are initialized in $|0\rangle_n$, n reversal qubits in $|1\rangle_n$, and an auxiliary qubit in $|0\rangle$. The reversal qubits are kept in bitwise negated states of the original qubits by applying CNOT gates. Subsequently, multi-controlled rotation gates are employed to apply precise $R_y(\theta)$ operations to the auxiliary qubit, conditioned on the combined states of both the original and reversal qubits. For example, in the case of $n=2$, the proposed adaptive rotation circuit is illustrated in Fig. 7. When the original qubits are in $|10\rangle$, the reversal qubits are automatically in $|01\rangle$ due to the CNOT configuration. A controlled rotation gate is then activated based on this unique qubit configuration to apply the corresponding rotation $R_y(\theta_2)$ to the auxiliary qubit. This implementation achieves high-precision realization of the controlled rotation operator \mathcal{F} . However, this accuracy comes at the cost of increased circuit depth and significant gate complexity, as 2^n controlled rotation gates are added to the circuit, which may hinder scalability for larger n .

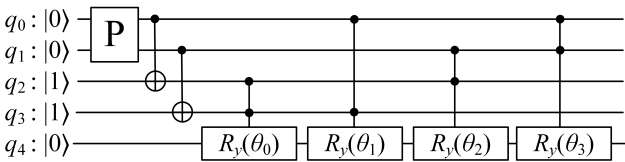


Fig. 7. Circuit-2 for precise implementation of \mathcal{F} .

Step 3-Quantum Amplitude Estimation: Based on (12), we can apply the QAE algorithm to estimate the amplitude

of the ancillary qubit being in $|1\rangle$, corresponding to the expectation of $\sum_{i=0}^{N-1} \hat{f}(i)p_i$.

For brevity, we summarize the fundamental idea of QAE as follows: consider a quantum system composed of n qubits in the state $|\psi\rangle_n$, along with an ancillary qubit initialized in the state $|0\rangle$. Let \mathcal{A} denote a quantum operator acting on the qubits:

$$\mathcal{A}|\psi\rangle_n|0\rangle = \sqrt{1-a}|\psi\rangle_n|0\rangle + \sqrt{a}|\psi\rangle_n|1\rangle. \quad (13)$$

QAE aims to estimate the probability of the “good” state $|1\rangle$ of the ancillary qubit, which is a . To achieve this goal, QAE employs the Grover operator $\mathcal{Q} = \mathcal{A}\mathcal{S}_0\mathcal{A}^\dagger\mathcal{S}_\chi$, where \mathcal{S}_0 is the operator for selective phase inversion of the initial state, and \mathcal{S}_χ is the operator for phase marking of the “good” state. The original amplitude estimation problem can be mapped to a phase estimation problem by iterative action on \mathcal{Q} . The amplitude $a \in [0, 1]$ is encoded as a rotation angle $\theta \in [0, \frac{\pi}{2}]$, satisfying $a = \sin^2(\theta)$, and renders (13) as:

$$\mathcal{A}|\psi\rangle_n|0\rangle = \cos(\theta)|\psi\rangle_n|0\rangle + \sin(\theta)|\psi\rangle_n|1\rangle. \quad (14)$$

By performing k iterations of the Grover operator \mathcal{Q} , the state of the ancillary qubit is transformed to:

$$\mathcal{Q}^k|\psi\rangle_n|0\rangle = \cos((2k+1)\theta)|\psi\rangle_n|0\rangle + \sin((2k+1)\theta)|\psi\rangle_n|1\rangle. \quad (15)$$

Thus, the probability of measuring the ancillary qubit in state $|1\rangle$ is $\sin^2((2k+1)\theta)$. When k is chosen to be $\lfloor \frac{\pi}{4\theta} \rfloor$, we have $\sin^2((2k+1)\theta) \approx 1$. Here, we achieve the amplitude amplification of the target state $|1\rangle$. It has been verified that the estimated value \tilde{a} satisfies $|\tilde{a} - a| \leq O(\frac{1}{M})$ with probability of at least $\frac{8}{\pi^2}$. M is the number of oracle queries. QAE algorithm has been verified to be able to achieve a quadratic speedup compared to the $O(\frac{1}{\sqrt{M}})$ convergence rate of classical MC methods [22], [23], where M is the number of MC simulations.

By applying QAE on (4), (4) can be computed efficiently.

IV. CASE STUDIES

A. Settings

A modified IEEE 33-bus distribution network integrated with DGs, uncertain loads, and multi-type ECs is adopted as the test system. One WT and two PVs are connected to buses 5, 11, and 31, respectively. Uncertain loads are located at buses 10, 12, and 14, while the remaining loads are assumed to be deterministic. Three industrial, commercial, and residential EC are connected to buses 7, 15, and 18, respectively. The voltage magnitude is restricted as $|V_i| \in [0.90, 1.10]$ (p.u.), $\forall i \in \Omega^N$. $\Delta t = 15$ min and $T = 96$. $\lambda = 1$ and $\alpha = 0.95$. The VQC for Q-TCN model uses 8 qubits and 3 layers. The VQC in Q-LSTM cell uses a hidden size of 3 and 2 recurrent layers. The learning rate is set as 0.01. Three datasets comprising 10,240 incentive-response samples from three ECs are generated using the models provided in Appendix A and utilized to train the proposed mapping model. Note that since modeling complex ECs' response behaviors is not the focus of this work, the models are simplified in form. Nevertheless, the proposed quantum learning and estimation approach remains applicable to more complex cases. QNNs are implemented using PennyLane, Jax, and Flaxnn libraries. QAE is implemented using Qiskit library. All computations

are implemented in Python 3.10.11, conducted on a Windows 11 64-bit operating system with an Intel Core i9-13900HX @ 2.30 GHz processor and 16 GB RAM.

B. Performance of Q-TCN-LSTM

In this part, we evaluate the performance of Q-TCN-LSTM in terms of accuracy and computational efficiency. The loss curves of the classical TCN-LSTM and Q-TCN-LSTM models on the test set during the training process are presented in Fig. 8. As observed, both models exhibit a rapid decrease in loss during the initial training epochs, followed by a gradual decline towards a stable convergence. This behavior highlights the effectiveness of the combined short-term and long-term temporal feature extraction capabilities of both the TCN-LSTM and Q-TCN-LSTM models. TCN-LSTM achieves convergence at around 25 epochs, with a final MSE loss of 0.013. In contrast, the Q-TCN-LSTM model demonstrates faster convergence at around 10 epochs and eventually reaches a relatively low MSE loss of 0.004. These results demonstrate the superior learning ability of the Q-TCN-LSTM model.

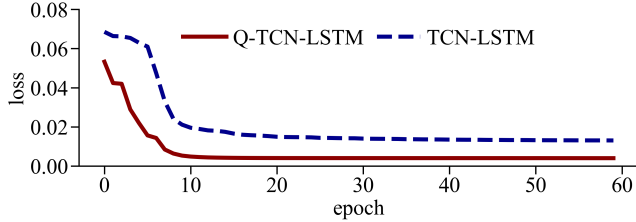


Fig. 8. Loss curves of TCN-LSTM and Q-TCN-LSTM on commercial EC.

To further illustrate the effectiveness of the Q-TCN-LSTM model in capturing the incentive-response behavior of ECs, we visualize two randomly selected response trajectories of the commercial EC from the test set, as shown in Fig. 9. The mapping results (blue dotted line) closely match the true values (red solid line) with minimal mapping deviation, demonstrating the model's high mapping precision and temporal generalization performance.

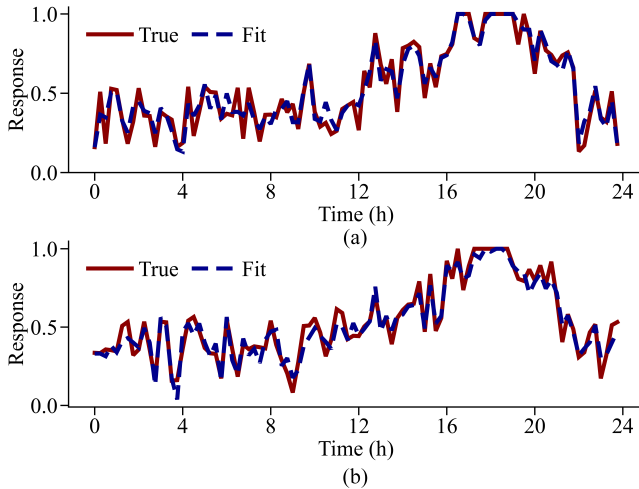


Fig. 9. Mapping results of two samples of commercial EC.

In addition, a comprehensive comparative experiment is conducted to further evaluate the superiority of Q-TCN-LSTM.

Classical neural networks (Multi-Layer Perceptron (MLP), TCN, LSTM, TCN-LSTM) and quantum neural networks (Q-MLP, Q-TCN, Q-LSTM) are included for comparison, as shown in Fig. 10.

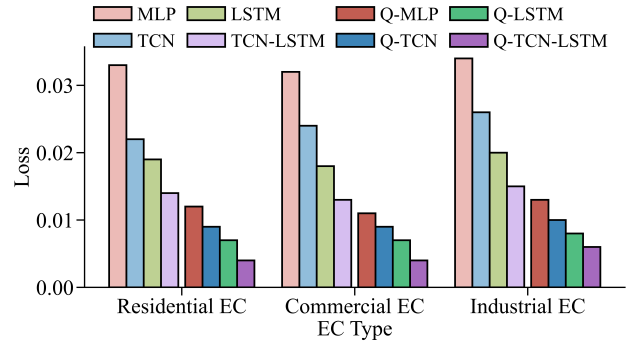


Fig. 10. Mapping performance comparison of multiple models.

As shown in Fig. 10, QNNs consistently outperform their classical counterparts across all three ECs, achieving lower loss and demonstrating superior function approximation capabilities. This advantage can be attributed to the unique properties of quantum computing. Specifically, quantum entanglement provides QNNs with powerful nonlinear expressive capabilities, enabling the effective modeling of complex relationships between pricing incentives and responses within ECs.

Among the QNN architectures evaluated, Q-TCN-LSTM achieves the highest mapping accuracy. This is primarily due to its hybrid architecture, which integrates the strengths of both Q-TCN and Q-LSTM networks. In Q-TCN, the integration of quantum convolutional layers with quantum parallelism enables the model to efficiently capture fine-grained temporal dependencies within short time sequences. The Q-LSTM leverages quantum superposition to significantly increase its memory capacity. This allows the model to maintain strong correlations between distant data points, leading to a better understanding of long-range context. By leveraging the strengths of both Q-TCN and Q-LSTM, the Q-TCN-LSTM architecture is capable of capturing both short-term and long-term temporal dependencies inherent in the EC response patterns, thereby enhancing its overall performance.

Moreover, we compare the computational efficiency of Q-TCN-LSTM with other models. Due to the current limitations in quantum hardware availability, all quantum operations are simulated on classical processors. We adopt the formula in [28] to approximate the quantum computational time: $T^Q = T^P + T^G \cdot D + T^M$, where T^P denotes state preparation time, T^G represents the average duration of a single quantum gate, D is the maximal circuit depth, and T^M is the quantum measurement time. Empirical values from [28] suggest that $T^P + T^M = 1 \mu s$ and $T^G = 10 ns$, which indicates that the time for state preparation and measurement takes much part of the total time. Thus, one execution time of the convolution operation in the VQC in Q-TCN takes around $1.1 \mu s$, which is much less than that of classical convolution and activation operation (around $18 \mu s$). This is because quantum parallelism enables performing multiple operations simultaneously, significantly boosting computational speed. In terms of model size, the

TCN-LSTM model has a total of 37353 parameters, while the Q-TCN-LSTM model uses only 94 parameters, approximately only 0.25% of the TCN-LSTM model's parameter count. Q-TCN-LSTM outperforms the classical TCN-LSTM while using far fewer parameters and operating at a much higher speed, demonstrating its high computational efficiency.

C. Performance of QAE

To validate the computational efficiency of quantum estimation methods for problems involving a large number of scenarios, we compare the estimation error (expressed as a percentage) and the corresponding computation time under varying numbers of MC samples and QAE qubits. The detailed results are illustrated in Fig. 11.

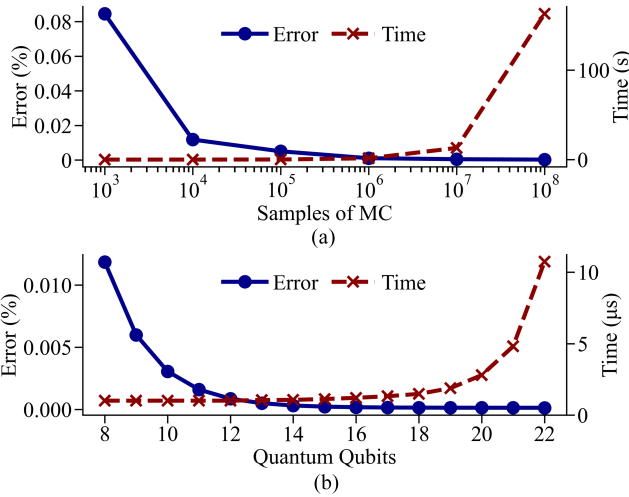


Fig. 11. Comparison of MC and QAE: (a) MC, (b) QAE with Circuit 1.

As shown in Fig. 11, MC achieves a low estimation error of approximately 0.001% with a substantial number of 10^6 samples, while QAE attains a comparable error level of 0.0008% with only 12 qubits. This demonstrates a substantial reduction in required computational resources. Moreover, QAE demonstrates a marked advantage in time efficiency. Under a similar error threshold (MC with 10^6 samples vs. QAE with 12 qubits), MC requires approximately 1.47 s of computation time, while QAE completes the task in approximately $0.01 \mu s$. This efficiency gain is primarily attributed to the quadratic speedup in query complexity offered by QAE. Furthermore, given the exponential growth of quantum circuit execution capacity with increasing qubits, the computational advantage of QAE is expected to become even more pronounced in large-scale estimation problems. Overall, these findings underscore the superiority of QAE in terms of both estimation accuracy and computational efficiency.

In addition, the performance of QAE using the approximate circuit (Circuit-1) and the precise circuit (Circuit-2) is compared in terms of estimation error and computational time, as shown in Table I. The results indicate that Circuit-1 does not exhibit notable increase in estimation error compared to Circuit-2. This is primarily due to the linearity of the function $\hat{f}(\cdot)$ in the current estimation task. In such cases, the corresponding quantum rotation angles can be effectively approximated by linear interpolation. However, if $\hat{f}(\cdot)$ exhibits

strong nonlinearity, the linear approximation of rotation angles might become inaccurate, leading to potentially higher estimation errors. In contrast, Circuit-2 can represent such functions with higher precision but at the cost of increased complexity: it requires $2n+1$ qubits and 2^n quantum controlled rotation gates, resulting in substantially higher execution time. Therefore, in practical applications, the choice between the two circuit designs should be guided by the functional characteristics of the estimation target and the required trade-off between accuracy and computational complexity.

TABLE I
PERFORMANCE COMPARISON OF CIRCUIT-1 AND CIRCUIT-2

| Circuit | Metric | Number of Qubits | | | | | | |
|-----------|------------------|------------------|--------|--------|--------|--------|--------|--------|
| | | 5 | 6 | 7 | 8 | 9 | 10 | 11 |
| Circuit-1 | Error (%) | 0.0939 | 0.0470 | 0.0236 | 0.0119 | 0.0060 | 0.0031 | 0.0016 |
| | Time (μs) | 0.0040 | 0.0060 | 0.0060 | 0.0060 | 0.0060 | 0.0061 | 0.0063 |
| Circuit-2 | Error (%) | 0.0937 | 0.0468 | 0.0234 | 0.0117 | 0.0058 | 0.0029 | 0.0014 |
| | Time (μs) | 0.1685 | 0.8326 | 4.8751 | 93.423 | 755.83 | 6534.4 | 58568 |

D. Result of DNs-ECs Coordination

In the optimization problem of DNs, the explicit gradient structure is established between the objective function and the decision variables, facilitating the search for the optimum. Thus, leveraging the accurate incentive-response mapping of ECs enabled by Q-TCN-LSTM, along with the accurate gradient estimation enabled by QAE, gradient descent can be efficiently employed. The bilevel DNs-ECs coordination optimization results are shown in Fig. 12.

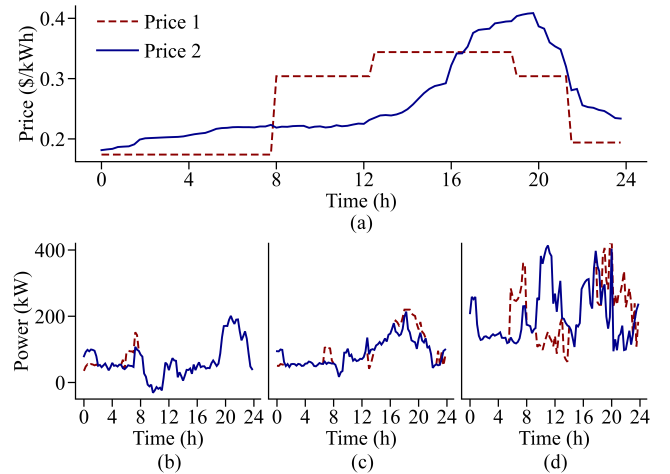


Fig. 12. Results of price and trading strategies of ECs: (a) Electricity trading price, (b) Residential EC, (c) Commercial EC, (d) Industrial EC.

As illustrated in Fig. 12, the optimized pricing scheme (Price 2) exhibits a more intricate and time-varying structure compared to the baseline fixed pricing (Price 1). This enables better alignment with the comprehensive load characteristics and operational profiles of multi-type ECs. Figure 12 indicates that Price 2 increases during 0-8 h and 16-24 h, while decreasing significantly during 8-16 h. This pricing pattern closely matches the underlying net load dynamics of the ECs: during 8-16 h, high penetration of renewable generation leads

to lower net loads, making it suitable to reduce electricity prices and encourage local consumption. Conversely, the 16-24 h period corresponds to the daily peak demand interval, where elevated prices are employed to suppress load aggregation and incentivize demand shifting. The effectiveness of this pricing scheme is further reflected in user response behavior, as shown in Fig. 12(b)-(d). Following price optimization, all three user types exhibit varying degrees of net load shifting, particularly during the high-price hours (16-24 h), resulting in a noticeable reduction in peak net loads. Among them, industrial users demonstrate the most substantial response due to their large and adjustable load capacity, indicating high sensitivity to price signals. Commercial users show moderate responsiveness, while residential users exhibit limited flexibility due to the inherent rigidity of their consumption patterns and fewer controllable loads. This coordinated response behavior effectively reduces the negative impact of ECs on the DNs. After optimizing the pricing strategy, the average penalty cost of voltage violation decreases from 17.76 to 2.24, indicating the capacity of user-side response to alleviate potential risks and enhance distribution network reliability. Overall, leveraging the advantages of quantum computing, the DNs-ECs coordination optimization problem can be solved efficiently.

V. CONCLUSION

In this paper, a quantum learning and estimation approach is proposed to address the bilevel DNs-ECs coordination problem. By leveraging quantum properties including quantum superposition and entanglement, the proposed Q-TCN-LSTM model can efficiently learn the incentive-response characteristics of ECs, realizing accurate estimation of user electricity consumption behavior under limited information. Additionally, QAE is introduced to facilitate evaluations with numerous scenarios, achieving a quadratic speedup over classical MC methods, significantly reducing computational resource consumption and execution time. In this way, the proposed quantum learning and estimation approach efficiently facilitates the coordination between DNs and ECs to generate better pricing strategies to regulate the net load profiles of ECs, thereby reducing the operational risk introduced to the DNs. As illustrated by the case studies, the proposed quantum-enhanced approach demonstrates superior performance in terms of both mapping accuracy and computational efficiency.

Future work will consider integrating quantum generative adversarial networks for scenario generation into the quantum estimation process to further enhance the efficiency of estimation and optimization processes.

APPENDIX

A. Operation Model of Multi-Type ECs

Different types of ECs exhibit heterogeneous characteristics in terms of device composition and operational preferences, leading to diverse operational behaviors.

1) *Residential ECs*: Residential ECs (e.g., individual households, apartment complexes, and community clusters) typically integrate rooftop PV systems, electric vehicles (EVs), inflexible loads (e.g., essential household appliances),

and flexible loads (e.g., air conditioners). Flexible loads are modeled with both temporal shiftability and power reducibility. EVs function as energy storage (ES) to provide ancillary service through smart charging/discharging. However, due to daily commuting patterns, EVs are typically unavailable during daytime hours and can only participate in energy management during night. Additionally, charging and discharging cycles are constrained to mitigate battery degradation.

The objective of residential ECs operation is to minimize the total operational cost. Thus, the overall operation model of residential ECs is formulated as follows:

$$\min \sum_{t=1}^T \pi_t^{\text{EC}} P_t^{\text{EX,R}} \Delta t, \quad (16a)$$

$$\text{s.t. } 0 \leq P_t^{\text{E,c}} \leq D_t^{\text{E,c}} \bar{P}^{\text{E}}, 0 \leq P_t^{\text{E,d}} \leq D_t^{\text{E,d}} \bar{P}^{\text{E}}, \forall t \in \mathcal{T}, \quad (16b)$$

$$0 \leq D_t^{\text{E,c}} + D_t^{\text{E,d}} \leq 1, \forall t \in \mathcal{T}, \quad (16c)$$

$$\text{SoC}_{t+1} = \text{SoC}_t + \Delta t (P_t^{\text{E,c}} \eta^{\text{c}} - P_t^{\text{E,d}} / \eta^{\text{d}}) / E, \forall t \in \mathcal{T}, \quad (16d)$$

$$\underline{\text{SoC}} \leq \text{SoC}_t \leq \overline{\text{SoC}}, \forall t \in \mathcal{T}, \quad (16e)$$

$$\text{SoC}_{t_1} = \overline{\text{SoC}}, \text{SoC}_{t_2} = \underline{\text{SoC}}, \quad (16f)$$

$$P_t^{\text{E,c}} = 0, P_t^{\text{E,d}} = 0, \forall t \notin \mathcal{T}, \quad (16g)$$

$$0 \leq \sum_{t \in \mathcal{T}} (D_t^{\text{E,c}} + D_t^{\text{E,d}}) \leq N^{\text{E}}, \quad (16h)$$

$$-\rho \hat{P}_t^{\text{L}} \leq P_t^{\text{L,s}} \leq \rho \hat{P}_t^{\text{L}}, \quad (16i)$$

$$0 \leq P_t^{\text{R,c}} \leq \hat{P}_t^{\text{R}}, \quad (16j)$$

$$P_t^{\text{EX,R}} = -(\hat{P}_t^{\text{R}} - P_t^{\text{R,c}}) + \hat{P}_t^{\text{L}} + P_t^{\text{L,s}} + P_t^{\text{E,c}} - P_t^{\text{E,d}}, \quad (16k)$$

$$\underline{P}_t^{\text{EX,R}} \leq P_t^{\text{EX,R}} \leq \overline{P}_t^{\text{EX,R}}, \quad (16l)$$

where (16b)-(16c) constrain the charging/discharging power (i.e., $P_t^{\text{E,c}}/P_t^{\text{E,d}}$) limited by \bar{P}^{E} and state (i.e., $D_t^{\text{E,c}}/D_t^{\text{E,d}}$) of ES. (16d)-(16f) further regulate the state of charge (SoC) dynamics with charging/discharging efficiency $\eta^{\text{c}}/\eta^{\text{d}}$ and ES capacity E . (16f) enforces that the SoC reaches its upper bound (i.e., $\overline{\text{SoC}}$) at the end of the nighttime (i.e., t_1), and its lower bound (i.e., $\underline{\text{SoC}}$) at the end of the daytime (i.e., t_2), and (16g) constrains the time periods (i.e., $\mathcal{T} = [1, t_1] \cup [t_2, T]$) when ES is not allowed to charge/discharge. (16h) limits the total number of charging/discharging operations (i.e., N^{E}) to reduce battery degradation. (16i) constrains the flexible load shedding (i.e., $P_t^{\text{L,s}}$) of the forecasted load demand (i.e., \hat{P}_t^{L}). (16j) constrains the maximum energy curtailment (i.e., $P_t^{\text{R,c}}$) of the forecasted renewable energy generation (i.e., \hat{P}_t^{R}). (16k) is the power balance equation. $P_t^{\text{EX,R}}$ is the trading power of the residential EC limited by the upper bound $\overline{P}_t^{\text{EX,R}}$ in (16l). $\Delta t/T$ are the scheduling time interval/total time period. ρ is the maximum shedding ratio of the flexible load reflecting the response willingness of the user.

2) *Commercial ECs*: Commercial ECs (e.g., shopping malls, office buildings, and hotels) are considered to be equipped with PV, ES, inflexible loads and flexible loads. Due to their customer-oriented operational nature, flexible loads in commercial ECs are typically restricted to curtailment rather than shifting. Such adjustments are often associated with customer discomfort or service quality degradation, which can lead to additional economic costs.

The objective of commercial ECs operation is to minimize the operational cost including the power trading cost and the flexible load adjustment cost. Thus, the overall operation model of commercial ECs is given as follows:

$$\min \sum_{t=1}^T \Delta t (\pi_t^{\text{EC}} P_t^{\text{EX,C}} + \alpha^{\text{L,S}} P_t^{\text{L,S}}), \quad (17a)$$

$$\text{s.t. (16b)–(16e), (16j), } \forall t \in [1, T], \quad (17b)$$

$$\sum_{t=1}^T (P_t^{\text{E,c}} \eta^{\text{c}} - P_t^{\text{E,d}} / \eta^{\text{d}}) \Delta t = 0, \quad (17c)$$

$$0 \leq P_t^{\text{L,S}} \leq \rho \hat{P}_t^{\text{L}}, \quad (17d)$$

$$P_t^{\text{EX,C}} = -(\hat{P}_t^{\text{R}} - P_t^{\text{R,c}}) + \hat{P}_t^{\text{L}} - P_t^{\text{L,S}} + P_t^{\text{E,c}} - P_t^{\text{E,d}}, \quad (17e)$$

$$\underline{P}_t^{\text{EX}} \leq P_t^{\text{EX,C}} \leq \bar{P}_t^{\text{EX}}, \quad (17f)$$

where (17c) denotes period constraint of the ES. $\alpha^{\text{L,S}}$ is the flexible load adjustment cost coefficient. $P_t^{\text{EX,C}}$ is the trading power of the commercial ECs.

3) *Industrial ECs*: Industrial ECs (e.g., manufacturing, mining, and construction industries) are typically equipped with PV, energy storage, inflexible load, flexible load, and distributed generator (DG). Considering the complex operational characteristics of industrial production processes, flexible loads exist in the form of discrete entire processes and can only be shifted as a whole in terms of temporal sequence.

The objective of industrial ECs operation is to minimize the operational cost including cost for power trading, flexible load adjustment, RES reduction and DG generation. Thus, the overall operation model of industrial ECs is as follows:

$$\min \sum_{t=1}^T \Delta t (\pi_t^{\text{EC}} P_t^{\text{EX,I}} + \alpha^{\text{DG}} P_t^{\text{DG}} + \sum_{i=1}^{N^{\text{s}}} \alpha_i^{\text{L,S}} P_{i,t}^{\text{L,S}} \Delta t_i^{\text{L,S}} + \alpha^{\text{R,c}} P_t^{\text{R,c}}), \quad (18a)$$

$$\text{s.t. (16b)–(16e), (17c), (16j), } \forall t \in [1, T], \quad (18b)$$

$$0 \leq P_t^{\text{DG}} \leq \bar{P}^{\text{DG}}, \quad (18c)$$

$$-\Delta \bar{P}^{\text{DG}} \leq P_t^{\text{DG}} - P_{t-1}^{\text{DG}} \leq \Delta \bar{P}^{\text{DG}}, \quad (18d)$$

$$\tilde{P}_{i,t-\Delta t_i^{\text{L,S}}}^{\text{L,S}} = P_{i,t}^{\text{L,S}}, \quad \forall t \in [t_i^1, t_i^2], \quad \forall i \in [1, N^{\text{s}}], \quad (18e)$$

$$\tilde{P}_t^{\text{L}} = P_t^{\text{L}} - \sum_{i=1}^{N^{\text{s}}} P_{i,t}^{\text{L,S}} + \sum_{i=1}^{N^{\text{s}}} \tilde{P}_{i,t}^{\text{L,S}}, \quad (18f)$$

$$P_t^{\text{EX,I}} = -(P_t^{\text{R}} - P_t^{\text{R,c}}) + \tilde{P}_t^{\text{L}} + P_t^{\text{E,c}} - P_t^{\text{E,d}} - P_t^{\text{DG}}, \quad (18g)$$

$$\underline{P}_t^{\text{EX}} \leq P_t^{\text{EX,I}} \leq \bar{P}_t^{\text{EX}}, \quad (18h)$$

where P_t^{DG} is the DG output power, and $\bar{P}^{\text{DG}} / \Delta \bar{P}^{\text{DG}}$ denote its maximum output/ramping limit. a, b are the DG cost coefficients. \tilde{P}_t^{L} is the adjusted load demand. $\tilde{P}_{i,t}^{\text{L,S}} / \Delta t_i^{\text{L,S}}$ are the adjusted power and duration of the i -th flexible load (N^{s} in total), where t_i^1 / t_i^2 denote the start/end time periods.

REFERENCES

- [1] B. Chen, J. Wang, X. Lu *et al.*, “Networked microgrids for grid resilience, robustness, and efficiency: A review,” *IEEE Trans. on Smart Grid*, vol. 12, no. 1, pp. 18–32, 2021.
- [2] T. Xu, R. Wang, H. Meng *et al.*, “A coordinated two-stage decentralized flexibility trading in distribution grids with mgs,” *Protection and Control of Modern Power Systems*, vol. 9, no. 5, pp. 54–69, 2024.
- [3] Y. Wang, M. Jia, N. Gao *et al.*, “Federated clustering for electricity consumption pattern extraction,” *IEEE Trans. on Smart Grid*, vol. 13, no. 3, pp. 2425–2439, 2022.
- [4] N. Qi, L. Cheng, H. Xu *et al.*, “Smart meter data-driven evaluation of operational demand response potential of residential air conditioning loads,” *Applied Energy*, vol. 279, p. 115708, 2020.
- [5] X. Zhang, G. Hug, and I. Harjunkoski, “Cost-effective scheduling of steel plants with flexible eafs,” *IEEE Trans. on Smart Grid*, vol. 8, no. 1, pp. 239–249, 2017.
- [6] J. Zhong, Y. Li, Y. Wu *et al.*, “Optimal operation of energy hub: An integrated model combined distributionally robust optimization method with stackelberg game,” *IEEE Trans. on Sustainable Energy*, vol. 14, no. 3, pp. 1835–1848, 2023.
- [7] N. T. Dinh, S. Karimi-Arpanahi, R. Yuan *et al.*, “Modeling irrational behavior of residential end users using non-stationary gaussian processes,” *IEEE Trans. on Smart Grid*, vol. 15, no. 5, pp. 4636–4648, 2024.
- [8] C. Lu, J. Cui, H. Wang *et al.*, “Privacy preserving user energy consumption profiling: From theory to application,” *IEEE Trans. on Smart Grid*, vol. 15, no. 2, pp. 2332–2347, 2024.
- [9] Y. Wang, Q. Chen, T. Hong *et al.*, “Review of smart meter data analytics: Applications, methodologies, and challenges,” *IEEE Trans. on Smart Grid*, vol. 10, no. 3, pp. 3125–3148, 2019.
- [10] A. Mallick, A. Mishra, A. R. Hota *et al.*, “Distributed coordination of multi-microgrids in active distribution networks for provisioning ancillary services,” *IEEE Systems Journal*, vol. 18, no. 3, pp. 1492–1503, 2024.
- [11] Y. Du and F. Li, “Intelligent multi-microgrid energy management based on deep neural network and model-free reinforcement learning,” *IEEE Trans. on Smart Grid*, vol. 11, no. 2, pp. 1066–1076, 2020.
- [12] Y. Bahri, E. Dyer, J. Kaplan *et al.*, “Explaining neural scaling laws,” *Proceedings of the National Academy of Sciences*, vol. 121, no. 27, p. e2311878121, 2024.
- [13] A. J. Kleywegt, A. Shapiro, and T. Homem-de Mello, “The sample average approximation method for stochastic discrete optimization,” *SIAM Journal on Optimization*, vol. 12, no. 2, pp. 479–502, 2002.
- [14] D. Xiao, H. Chen, W. Cai *et al.*, “Integrated risk measurement and control for stochastic energy trading of a wind storage system in electricity markets,” *Protection and Control of Modern Power Systems*, vol. 8, no. 4, pp. 1–11, 2023.
- [15] J. Zhang, “Modern monte carlo methods for efficient uncertainty quantification and propagation: A survey,” *WIREs Computational Statistics*, vol. 13, no. 5, p. e1539, 2021.
- [16] Y. Zhuang, L. Cheng, N. Qi *et al.*, “Problem-driven scenario reduction framework for power system stochastic operation,” *IEEE Trans. on Power Systems*, pp. 1–14, 2024.
- [17] T. D. Ladd, F. Jelezko, R. Laflamme *et al.*, “Quantum computers,” *Nature*, vol. 464, no. 7285, pp. 45–53, 2010.
- [18] D. Herman, C. Googin, X. Liu *et al.*, “Quantum computing for finance,” *Nature Reviews Physics*, vol. 5, no. 8, pp. 450–465, 2023.
- [19] Y. Y. Hong and J. B. D. Santos, “Day-ahead spatiotemporal wind speed forecasting based on a hybrid model of quantum and residual long short-term memory optimized by particle swarm algorithm,” *IEEE Systems Journal*, vol. 17, no. 4, pp. 6081–6092, 2023.
- [20] Y. Cao, X. Zhou, X. Fei *et al.*, “Linear-layer-enhanced quantum long short-term memory for carbon price forecasting,” *Quantum Machine Intelligence*, vol. 5, no. 2, p. 26, 2023.
- [21] A. Ajagekar and F. You, “Quantum computing based hybrid deep learning for fault diagnosis in electrical power systems,” *Applied Energy*, vol. 303, p. 117628, 2021.
- [22] P. Glasserman, P. Heidelberger, and P. Shahabuddin, “Efficient monte carlo methods for value-at-risk,” 2000.
- [23] G. Brassard, P. Høyer, M. Mosca *et al.*, “Quantum amplitude amplification and estimation,” p. 53–74, 2002.
- [24] E. Jong, B. Sævarsson, H. Jóhannsson *et al.*, “Quantum amplitude estimation for probabilistic methods in power systems,” *arXiv preprint arXiv:2309.17299*, 2023.
- [25] H. Yang, Y. Liu, Y. Yue *et al.*, “Power system reliability assessment technique and modeling approach based on quantum computing theory,” *Electric Power Systems Research*, vol. 236, p. 110957, 2024.
- [26] N. Nikmehr and P. Zhang, “Quantum-inspired power system reliability assessment,” *IEEE Trans. on Power Systems*, vol. 38, no. 4, pp. 3476–3490, 2023.
- [27] G. Brassard, P. Hoyer, M. Mosca *et al.*, “Quantum amplitude amplification and estimation,” *arXiv preprint quant-ph/0005055*, 2000.
- [28] G. G. Guerreschi and A. Y. Matsuura, “Qaoa for max-cut requires hundreds of qubits for quantum speed-up,” *Scientific Reports*, vol. 9, no. 1, p. 6903, 2019.